Global behaviour of a composite stiffened panel in buckling. Part 2: Experimental investigation

Adrien Perret, Sébastien Mistou, Marina Fazzini, Romain Brault

Global behaviour of a composite stiffened panel in buckling. Part 2: Experimental investigation

Adrien Perret [a,b], Sébastien Mistou [b], Marina Fazzini [b,*], Romain Brault [b]

[a] DAHER–SOCATA, Aéroport Tarbes-Lourdes-Pyrénées, 65290 Louey, France
[b] ENIT–LGP, PRES Université de Toulouse, Av. Azereix, BP1629, 65016 Tarbes, France

Keywords:
Structural composites
Fracture
Post-buckling
DIC
NDT

A B S T R A C T

The present study analyses an aircraft composite fuselage structure manufactured by the Liquid Resin Infusion (LRI) process and subjected to a compressive load. LRI is based on the moulding of high performance composite parts by infusing liquid resin on dry fibres instead of prepreg fabrics or Resin Transfer Moulding (RTM). Actual industrial projects face composite integrated structure issues as a number of structures (stiffeners, ...) are more and more integrated onto the skins of aircraft fuselage.

A post-buckling test of a composite fuselage representative panel is set up, from numerical results available in previous works. Two stereo Digital Image Correlation (DIC) systems are positioned on each side of the panel, that are aimed at correlating numerical and experimental out-of-plane displacements (corresponding to the skin local buckling displacements of the panel). First, the experimental approach and the test facility are presented. A post-mortem failure analysis is then performed with the help of Non-Destructive Techniques (NDT). X-ray Computed Tomography (CT) measurements and ultrasonic testing (US) techniques are able to explain the failure mechanisms that occured during this post-buckling test. Numerical results are validated by the experimental results.

1. Introduction

A representative test of a panel can be specified in terms of a compressive [1,2] or shear loading state [3]. A pressurised test at the panel level is more difficult to assess since it needs a combined loading [4]. Several studies can be found concerning a compressive post-buckling test of co-cured or co-bonded stiffened panels, manufactured in prepregs. It is known that opposite buckling waves – symmetric or antisymmetric – are the areas, where delamination initiates [5,6], leading to the loss of connection between skin and stiffeners [1]. In the case of excellent bonding, severe stress concentrations may cause delaminations and fracture in the skin or in the stiffener flanges at these locations [1].

This paper is the experimental investigation of a previous work which was the numerical modelling of this panel [7]. It aims to show the particular behaviour of a panel manufactured by a resin infusion process [8]. Numerical models consider the failure initiation anywhere through the thickness, rather than the damage initiates at the interface. A conventional testing machine can highlight the decohesion phenomenon in the skin–stiffener interface, by a uni-axial compressive test that makes the panel buckles. No strain gages are used because the displacement fields serve at correlating the numerical and experimental results through the use of stereo-DIC techniques, being tried and tested at the laboratory for more than 10 years.

Before the test, a newly made model that takes into account a layup modification of the stiffeners has led to redefine the load at collapse F_{max} = 127.026 kN for a shortening UX = 2.40 mm. This model is defined as the reference model. The load at collapse will be used to set-up the test. Geometric imperfections of the skins are not considered since they have an almost negligible effect on the load at collapse [9]. The side stiffeners provide enough rigidity so that the panel borders do not buckle [7].

The critical buckling load F_{cr} (corresponding to skin local buckling) has been recalculated by the linear buckling analysis [7] on the reference model. It equals 90.4 kN, which is close to the end of the linear behaviour in the non linear analysis, where F_{cr} is approximately 90 kN. Now, numerical results are concordant with the buckling mechanism [10]: from the critical buckling load, the skin local buckling causes a load redistribution in the stiffeners until collapse, and the behaviour becomes nonlinear. Thus linear models cannot be used anymore.

These mechanisms given by numerical results need to be validated by experiment. First of all, the experimental test is set-up. The panel and the tool placement is carefully checked so that the

* Corresponding author. Address: Laboratoire Génie de Production, École Nationale d'Ingénieurs de Tarbes, Équipe Mécanique des Matériaux, des Structures et Procédés (M2SP), Av. Azereix, BP1629, 65016 Tarbes, France. Tel.: +335 62 44 27 00.
E-mail address: Marina.Fazzini@enit.fr (M. Fazzini).

doi:10.1016/j.compstruct.2011.07.029

panel is properly lined up with the load direction of the testing machine. Then numerical and experimental results are correlated through the out-of-plane displacement field (*UZ*) measured by two stereo-DIC measurement systems that are positioned on each side of the panel. X-ray CT and US techniques are used to analyse the failure zones on the panel surface and through the thickness of the stiffener flanges, allowing numerical and experimental results to be corroborated.

2. Methodologies

2.1. Experimental techniques

Experimental methods mainly use optical measurement systems from GOM® Software. Using Tritop, a photogrammetric software, distances are checked between primitive surfaces defined from reference points on the test panel and on the tool. ATOS is a digitising software that can complete Tritop information, it is used to make digitisation of the test panel, and more particularly of the resin blocks at both ends of the test panel.

Finally, ARAMIS is a measurement system more specifically dedicated to the stereo-correlation of the plane and out-of-plane displacement fields, which is used to correlate numerical and experimental results.

For failure analysis, two-dimensional X-ray images measured with a medical scanner are used to analyse the material density variations and to locate damaged sites on the test panel surface. A reflection US technique gives complementary results to locate the failure initiation through the thickness all along the flange areas.

2.2. Experimental test set-up definition

Final dimensions of the test panel are 870 mm in length and 509 mm in width [7]. Resin blocks are 60 mm high and 80 mm wide. The tool design is shown in Fig. 1. Each resin block is positioned between two squares located on a plate which is mounted on a base, directly attached to the loaded axis of the testing machine. There are slotted holes in the squares, allowing this tool to accept larger panel geometries.

2.2.1. Test set-up

Fig. 2 shows the experimental set-up of this post-buckling test. An Instron 1345 testing machine is used with a 500 kN load sensor accurate at 0.5% on the test range. Load is applied by monitoring the displacement at 1 mm/min by BlueHill 2 (an Instron® software). Optical measurements of the two Aramis systems are triggered each 3 s on load and displacement analogic signals. One Aramis system is on the skin side of the test panel while the other one is on its stiffener side.

The test panel surface is painted using a sponge to create the speckle, as shown in Fig. 3a, where a synthetic speckle shown in Fig. 3b has been taken as a model (created with a randomly

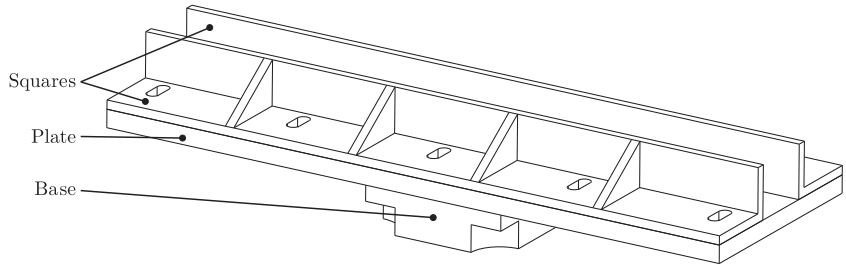

Fig. 1. Tool design of the post-buckling test.

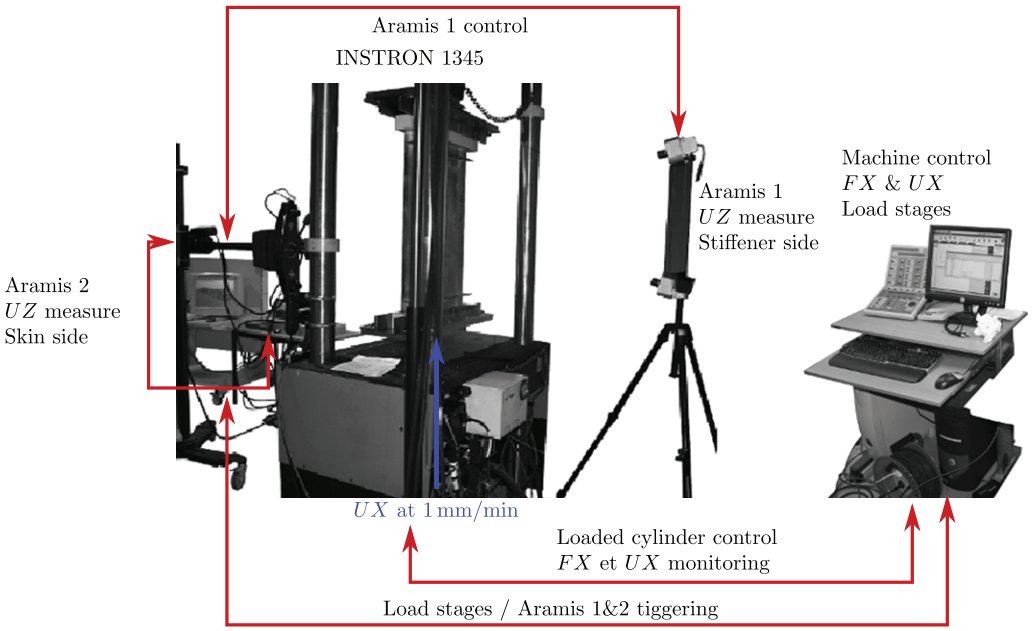

Fig. 2. Experimental set-up of the post-buckling test.

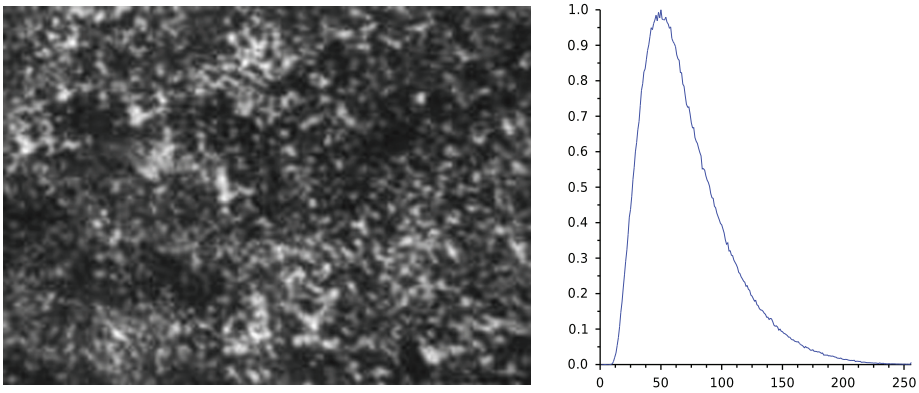

(a) Experimental speckle

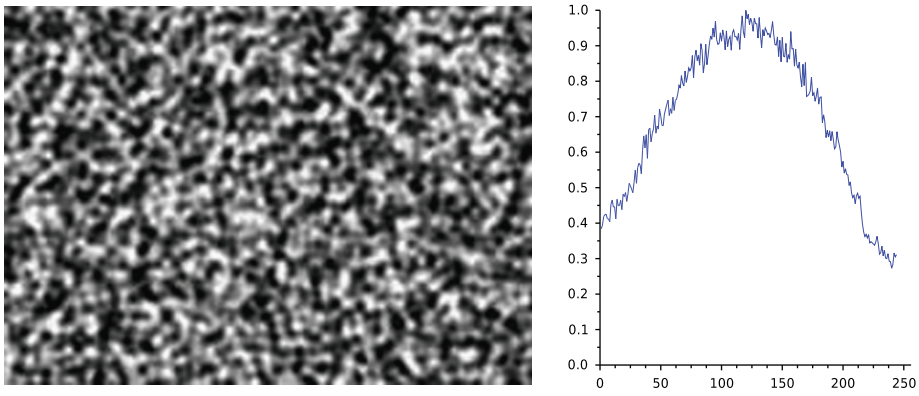

(b) Synthetic speckle

Fig. 3. Definition of the test panel speckles.

distributed grey levels). The experimental grey level distribution is close to a normal distribution. The speckle size is 2.1 pixels and 2.9 pixels for the optical system on the skin side and on the stiffener side respectively, with an optimal correlation window of 19 pixels and 28 pixels. One pixel is about 0.5 mm long.

2.2.2. Panel and tool check

Feedback from a first feasibility test brought to completion has permitted to underline steps to follow for the panel and the tool to be properly mounted on the testing machine.

After been manufactured by LRI (process not detailed here), the panel is machined to the final dimensions. Casting of an epoxy resin-calcium carbonate mix constitutes the resin blocks at each panel end. The panel is digitised to highlight geometric imperfections, more particularly the distance between resin blocks and the panel skin. Resin blocks are machined numerically to the final desired tolerances. A second digitisation gives the final geometric imperfections of the panel to be tested. Finally, a US control validates the test panel before its test.

Resin blocks are machined according to two critical parameters for the test to be set-up properly:

- The parallelism of the resin block ends, avoiding a misalignment of the load transmitted from the test device to the test panel.
- The flatness of the surface containing the resin block flanges, allowing the test panel to be perfectly vertical provided the resin block flange to the skin distance remains constant.

These two parameters are controlled by digitisation using Tritop after machining of the resin blocks, as shown in Figs. 4 and 5. A distance of 43.6 mm shall be found between the resin block

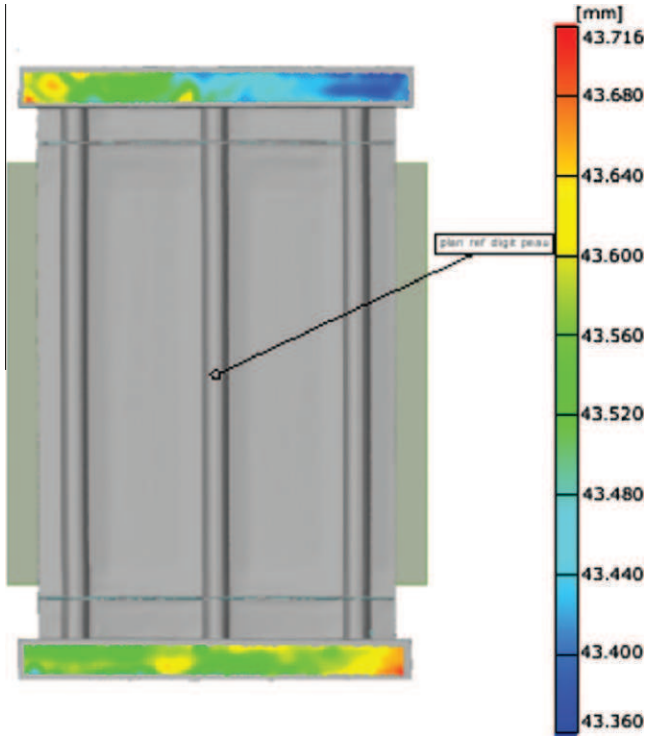

Fig. 4. Digitisations of the resin block flanges.

flanges and the skin. Fig. 4 shows that a ±0.18 mm gap exists between the lower and the upper resin flanges, considering a rotational degree of freedom of one panel end free about X (panel longitudinal axis). Fig. 5 gives the flatness of the upper and the lower block end surfaces of 0.14 mm and 0.10 mm respectively, for a parallelism of 0.37 mm.

The same two parameters are also checked on the tool side using the ATOS system to digitise reference points defined on the tool squares and plates. The measured parallelism of the square surfaces in Fig. 6a of nearly ±0.17 mm is on the same order as the measured gap of ±0.18 mm on the resin block flanges. The measured parallelism of the plate surfaces in Fig. 6b of nearly ±0.15 mm is nearly the half of the measured gap of ±0.37 mm on the resin block ends.

These two parameters are assumed to particularly affect a proper mounting of the panel and the tool. They allow test nonconformities to be defined, which are used to project the testing machine loading.

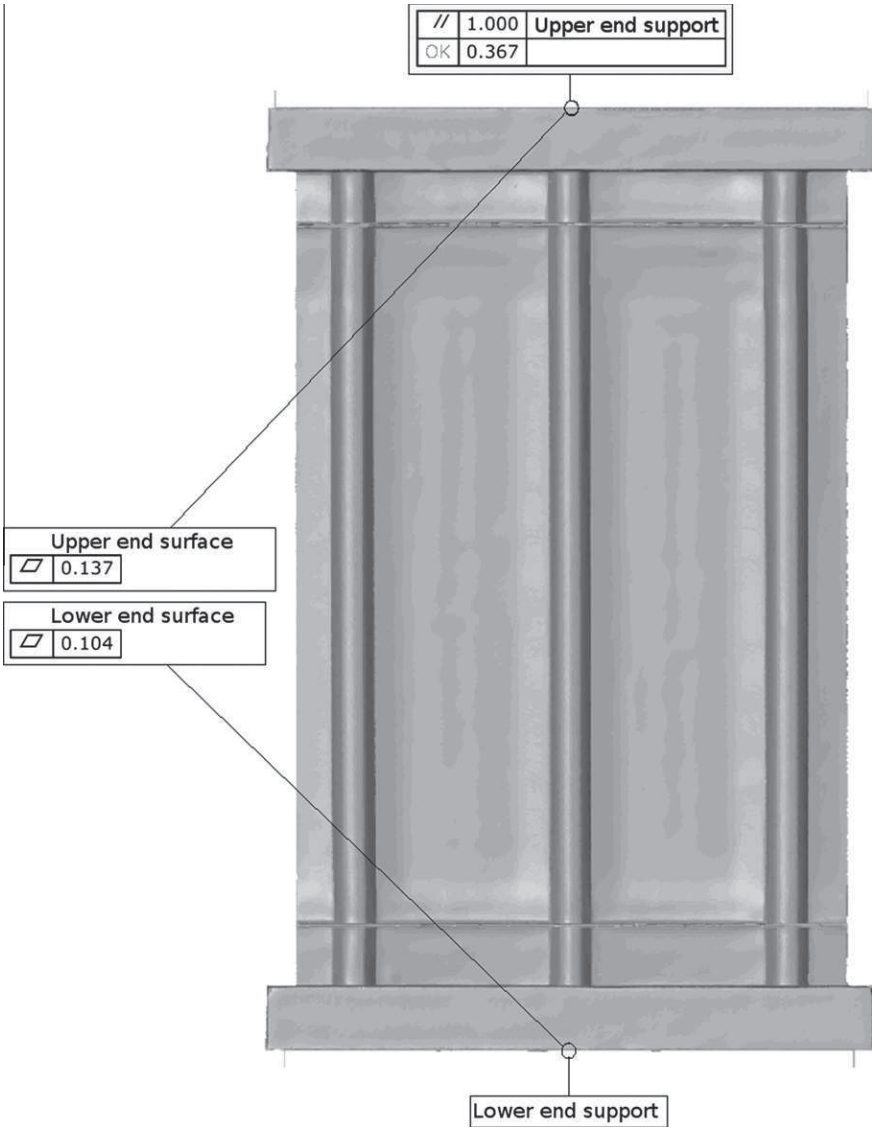

Fig. 5. Digitisations of the resin block end supports.

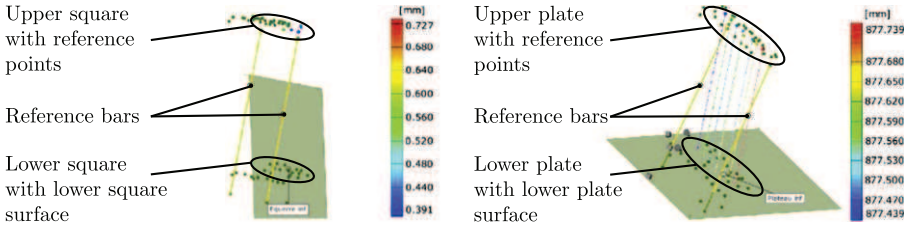

(a) Alignement of square surfaces (b) Alignement of plate surfaces

Fig. 6. Alignement of square and plate surfaces measured by photogrammetry.

2.2.3. Test nonconformities and projected loading

The test nonconformities have been introduced in the reference model to calculate their influence on the load at collapse F_{max}. They are introduced as a pre-load in displacement or in rotation at the loaded edge of the test panel. The most critical is the parallelism of the square surfaces which leads to decrease the load at collapse by 4.5% to nearly 121 kN.

As recommended by airworthiness standards [11], "The structure must be able to support ultimate loads without failure for at least 3 s [...]". Hence two loads are defined to help with setting fifteen load levels, where this 3 s time period is applied: the calculated load at collapse F_{max} = 128 kN which is the ultimate load *UL*, and the limit load *LL* = *UL*/1.5 which corresponds approximately to the critical buckling load at 85.3 kN (this 3 s time period is also defined in Section 2.2.1 to trigger optical measurement systems). One cycle up to about a load of 0.6 *LL* is also applied to settle misalignments in the test panel and in the test tool.

The projected loading is shown in Table 1. A load domain is defined ranging from 121 kN (most critical nonconformity) to 128 kN (calculated F_{max}), for which an indicator ☺ denotes a valid test. Considering a scatter on material properties leads to define a lower load of 106.7 kN and an upper load of 139.0 kN, where an indicator 😐 denotes an uncertain test. Finally, an indicator ☹ denotes a non valid test for a load falling outside of these ranges.

Table 1
Post-buckling test projected loading.

Level N°	*LL* ratio	Load (kN)	Indicator
1	0.60	51.2	☺
2	1.00	85.3	☺
3	1.10	93.9	☺
4	1.20	102.4	☺
5	1.25	106.7	😐
6	1.30	110.9	😐
7	1.34	114.3	😐
8	1.36	116.1	😐
9	1.38	117.8	😐
10	1.40	119.5	😐
11	1.42	121.2	☹
12	1.45	123.7	☹
13	1.50	128.0	☹
Forced failure		139.0	😐
		150.0	☺
Return to 0		0.0	–

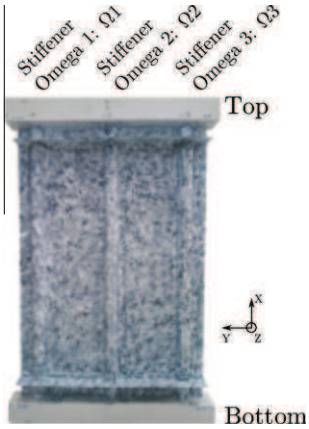

Fig. 8. Naming convention of the test panel.

3. Results and discussion

3.1. Numerical and experimental correlation

The test is achieved after the loading on the testing machine has been projected (Table 1) from the reference model.

The real relative longitudinal displacement (shortening) is calculated by Aramis using two reference points located below the central stiffener on the skin side, at the intersection between the panel skin and the resin blocks. These reference points must be defined along the central stiffener for the shortening to be correlated to the numerical curve. Fig. 7 shows the experimental and numerical curves with nine points used to discuss the results. The test has been witnessed by more than ten people, that attest the significance of the experimental results.

3.1.1. Experimental results

Essential experimental results are first the critical buckling load at nearly 90 kN which concords well with the linear buckling load as well as the beginning of the nonlinear behaviour found by the nonlinear analysis.

The load at collapse – used to project the loading – is found to be 126.630 kN, which means the gap between the numerical and the experimental load at collapse is included in the load sensor

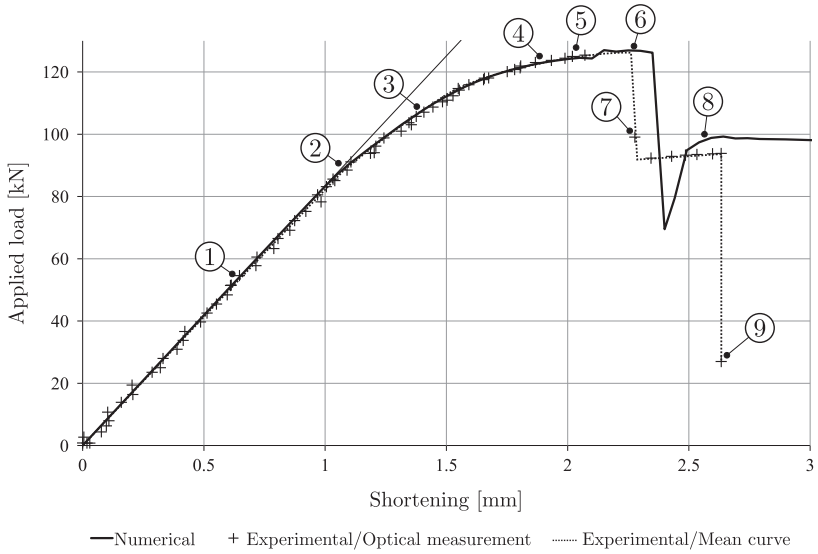

Fig. 7. Numerical and experimental load–shortening curves.

accuracy of 0.5% (comparing to 127.026 kN found by the nonlinear analysis). The shortening at collapse is 2.28 mm which is quite close to 2.40 mm calculated.

The post-buckling ratio is about $F_{max}/F_{cr} \approx 1.4$, which is relatively low comparing to values ranging from 2.9 to 6.0 for *T*-stiffened panels [1]. This could be explained by a possible load increase if the gliding conditions would be incorporated at panel borders, as well as a potential for the skin ply lay-up to be optimised.

For the following discussion, Fig. 8 shows the naming convention related to the upper and lower sides of the test panel and its three omega stiffeners Ω1, Ω2 and Ω3.

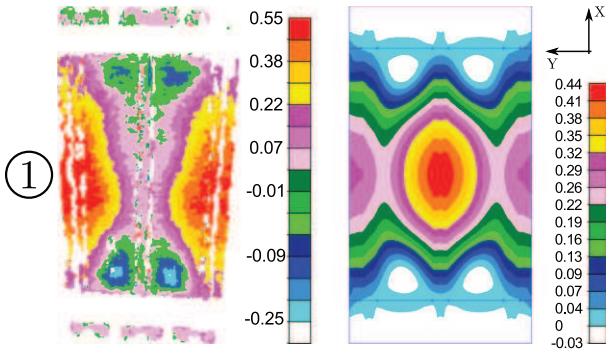

Fig. 9. Point 1 – linear stage.

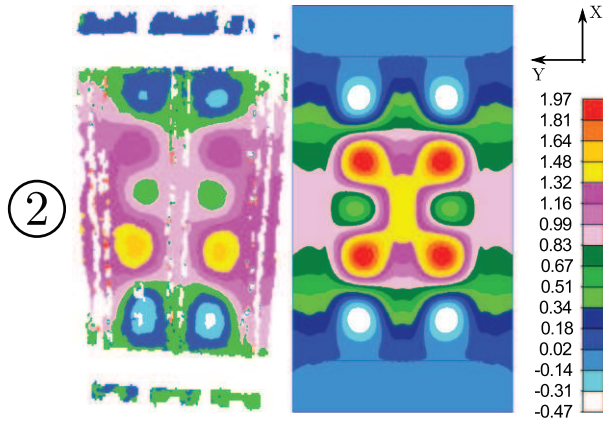

(a) Experimental and nonlinear results

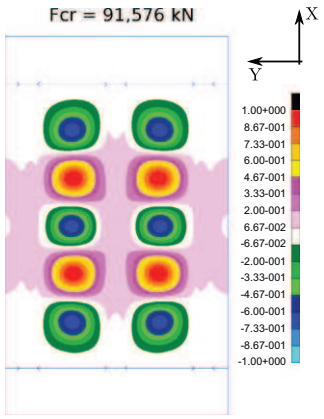

(b) Linear buckling load shape

Fig. 10. Point 2 – skin critical buckling load.

At each of the nine points shown in Fig. 7, the experimental out-of-plane displacement *UZ* mapping is shown on the left, while the numerical mapping appears on the right. These mappings are generally given for the stiffener side only with a similar scale.

3.1.2. Linear stage

During the linear stage for point 1 (Fig. 9), the loading is well correlated in terms of applied load and shortening. There is an amplitude reproducibility of the out-of-plane displacements. Two waves are formed at each panel ends until the load reaches the critical buckling load.

3.1.3. Skin critical buckling load

Out-of-plane displacement mapping at point 2 are shown in Fig. 10a. The experimental critical buckling load corresponds to skin local buckling at approximately 90 kN, which is concordant with the buckling mechanism [10]. Five symmetrical waves are formed on each panel skin as it has also been predicted by the linear buckling analysis (see Fig. 10b). From this critical buckling load, the behaviour becomes nonlinear and the linear analysis cannot be used anymore. The loading is then governed by the stiffener load carriage capacity.

This confirms the critical buckling load is correctly predicted by the numerical models [7], without introducing unit displacements – of the linear buckling eigenvalue – as a node displacement pre-load.

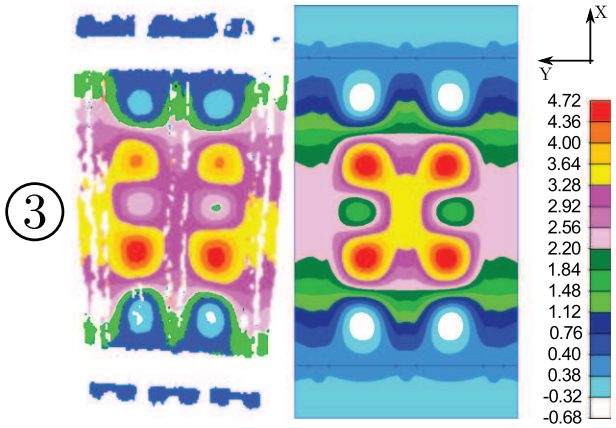

Fig. 11. Point 3 – beginning of the nonlinear stage.

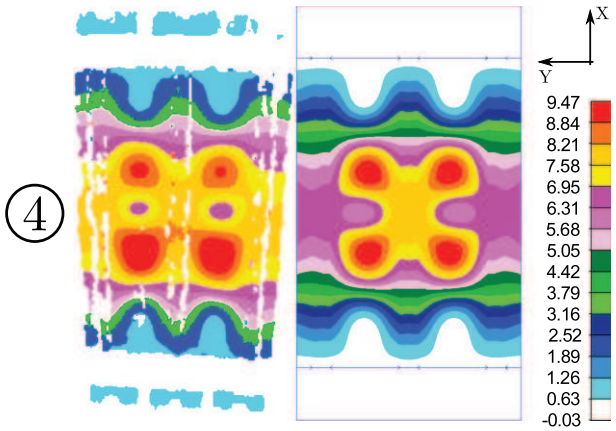

Fig. 12. Point 4 – advanced nonlinear stage.

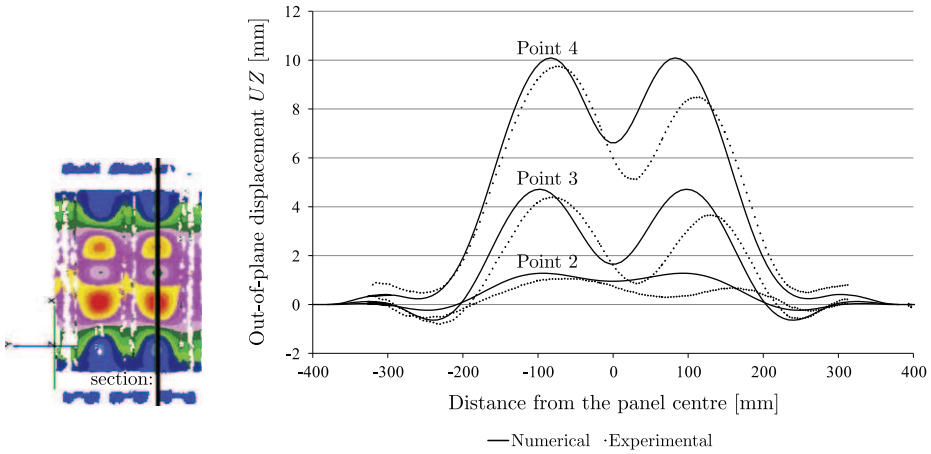

(a) Defined skin section

(b) Out-of-plane displacements UZ for the skin section in the length, at points 2, 3 and 4

Fig. 13. Out-of-plane displacement amplitude along the length of a skin section.

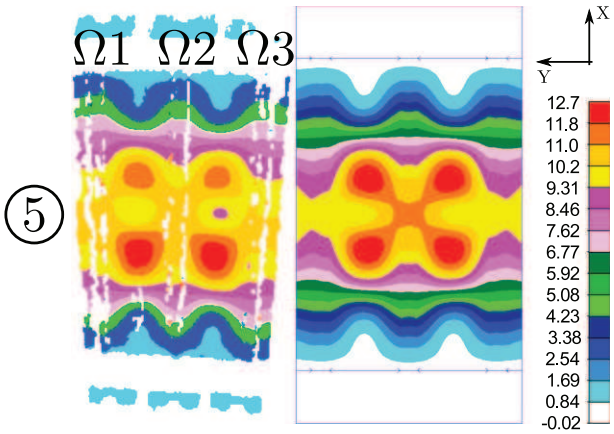

Fig. 14. Point 5 – last image of the projected loading.

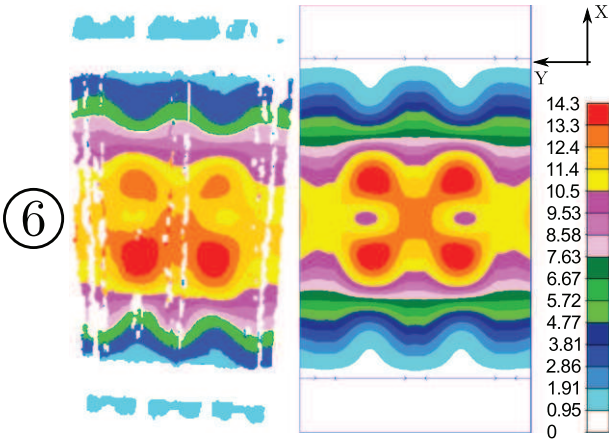

Fig. 15. Point 6 – last image before panel collapse.

3.1.4. Nonlinear stage – local →global buckling

During the nonlinear stage, Figs. 11 and 12 (Points 3 and 4 respectively) show the shape evolution of the out-of-plane displacements, where the skin local buckling mode is present and the panel seems to globally buckle when the nonlinear stage evolves.

This global buckling overlaying the skin local buckling mode can be evidenced by plotting the numerical and the experimental out-of-plane displacements for a given skin section along the length of the panel. The skin section is defined in Fig. 13a, and *UZ* is plotted at points 2, 3 and 4 in Fig. 13b. At point 2 the local buckling appears and only concerns the panel skins. At point 3 the skin local buckling has evolved and a global buckling is overlaid, resulting in a global out-of-plane displacement. At point 4, the global buckling has increased, but the skin buckling waves remain constant.

3.1.5. Load at collapse

Point 5 on Fig. 14 corresponds to the last image acquired by the measurement systems during the projected loading. At this point there is the recorded load at collapse of 126.630 kN.

The failure phenomenon is sudden – no experimental points are recorded during a shortening of 0.2 mm – and leads to notice a small desynchronisation between the two stereo-DIC systems connected in series. Fortunately, at the failure moment (points 6 and 7 in Figs. 15 and 16 respectively), the recorded image on the stiffener side indicates an healthy panel, while the recorded image

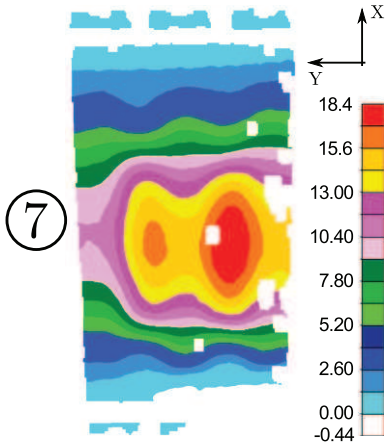

Fig. 16. Point 7 – first image after panel collapse.

on the skin side indicates a collapsed panel. Then one can conclude the experimental failure moment is at these points.

This failure moment results in a first load drop (as already seen in Fig. 7), and two failure noises are heard. Ω1 seems to be failed. Dust coming from its intersection led to have analysed the two consecutive recorded images at its upper and lower intersections. That confirmed this first load drop is caused by failure of its two intersections. These areas will be more specifically studied using non-destructive techniques.

To corroborate the panel collapse by Ω1 failure, three sections are defined on the omega heads, as shown in Fig. 17, to plot the out-of-plane *UZ* and the transversal displacements *UY* at the increment preceding and succeeding panel collapse.

Before collapse, Fig. 18a shows *UZ* of Ω2 is the largest as it is the central stiffener and the panel is globally buckled. After collapse on Fig. 18b, *UZ* of Ω1 becomes the largest because it does not carry any more load and the panel globally buckles with it. *UZ* of Ω1 and Ω2 have increased of nearly 7 mm and 4 mm respectively, while *UZ* of Ω3 has only increased by 0.5 mm.

The study of the transversal displacements *UY* in Fig. 19 confirms Ω1 failure. Before collapse, the central stiffener Ω2 being on the panel axis of symmetry, its transversal displacement *UY* is zero as seen in Fig. 19a. After collapse, Fig. 19b shows Ω2 is decentered in the Ω3 direction. Ω1 transversal displacement is now zero, showing that it does not carry any more load after the panel collapses.

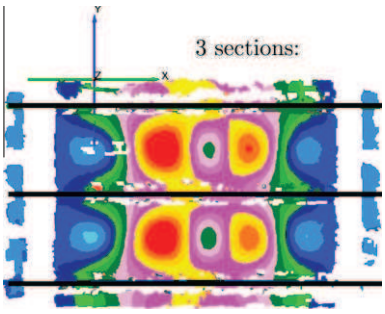

Fig. 17. Section definition on the omega heads.

3.1.6. Load plateau

After the first load drop, Ω1 is failed and it remains only two stiffeners to carry the load. That explains why, at the load plateau, the applied load becomes two-thirds of the load at collapse. The load threshold has not been detected by the test machine, which continued to load the panel.

Fig. 20 shows the panel buckles globally on the stiffener side. Ω2 and Ω3 are buckled but are not failed. The out-of-planes displacements given by the numerical models are no more consistent since failure is predicted for most areas at the first load drop.

Quite quickly, Ω2 and Ω3 failure occurs following another failure modes.

3.1.7. Ω2 and Ω3 decohesion

Fig. 21a shows the out-of-plane displacements of point 9, once Ω2 and Ω3 have delaminated as shown with a photography in Fig. 21b.

Two-thirds of the load capacity left are lost, because Ω2 and Ω3 have delaminated. Delamination has initiated by crippling as it has already been observed for this kind of test [12]. The crippling is a

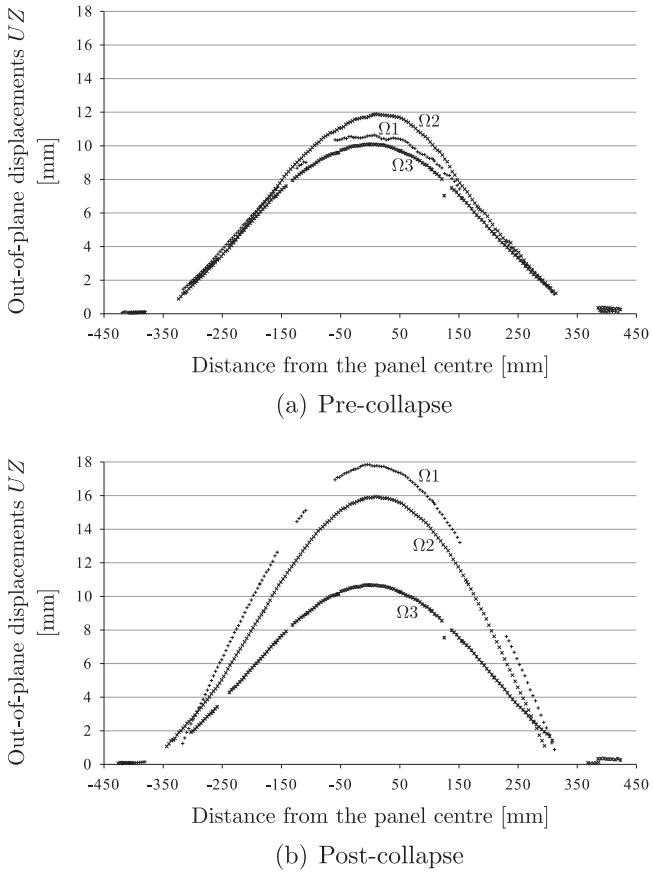

Fig. 18. Out-of-plane displacements *UZ* on omega heads.

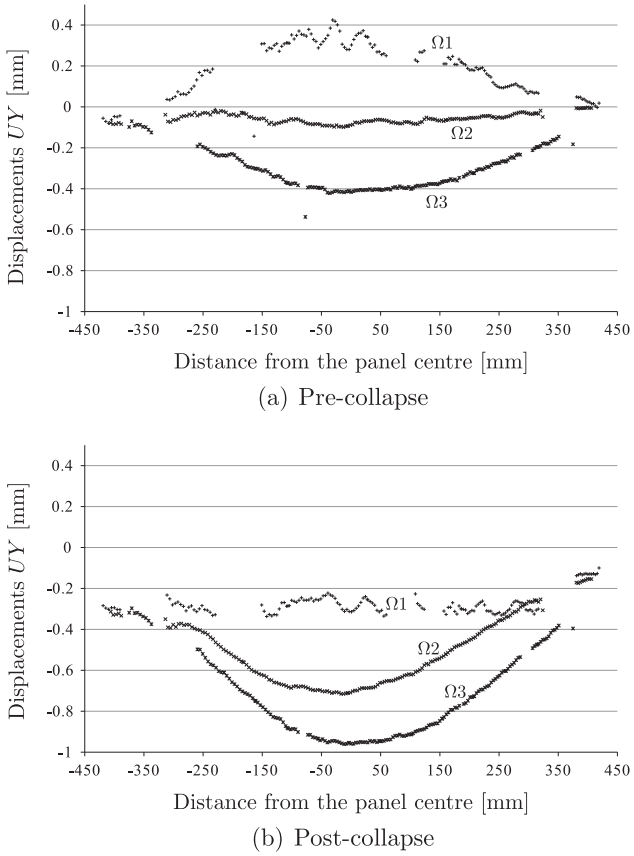

Fig. 19. Displacements *UY* on omega heads.

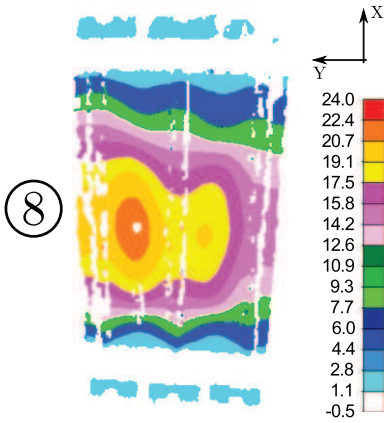

Fig. 20. Point 8 – stiffener side image at the load plateau.

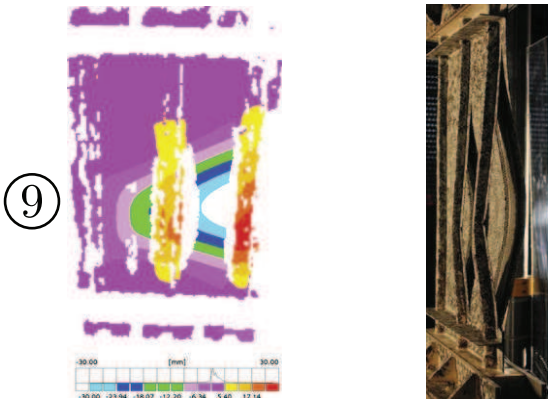

(a) Point 9 – last images after Ω2 and Ω3 decohesion

(b) Picture of the collapsed panel after Ω decohesion

Fig. 21. Point 9 – Ω2 and Ω3 decohesion.

local buckling phenomenon of closed structures. The crippling initiates at corners which are stiffers than other areas, because their rigidity allows them to carry the load once all local buckling loads are exceeded.

3.2. Failure analysis

3.2.1. Failure analysis using tomography

Tomographic measurements permit to study all of the local failure mechanisms that have occured during this post-buckling test. Fig. 22a shows four defects being identified on the panel surface. No delamination appears at Ω1 flanges while this is clearly visible for Ω2 and Ω3.

Defects 1 and 2 are located at the upper and at the lower Ω1 intersections (Fig. 22b), due to the first load drop. These defects appear as one crack at each stiffener head, that does not run through the whole stiffener thickness.

Defects 3 and 4 are the crippling failures of Ω2 and Ω3 (Fig. 22c), which have initiated their delamination. The loss of density coming from omega corners is consistent with this mode of failure initiation, where closed corners fail.

3.2.2. Failure analysis using US testing

A reflection US technique is used to locate the decohesion area through the thickness of the stiffener flanges, as shown in Fig. 23.

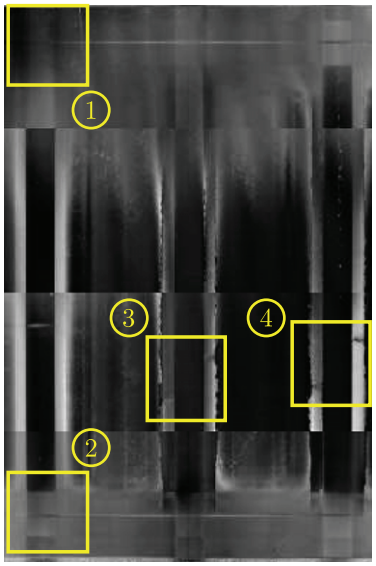

(a) tomographic cartography

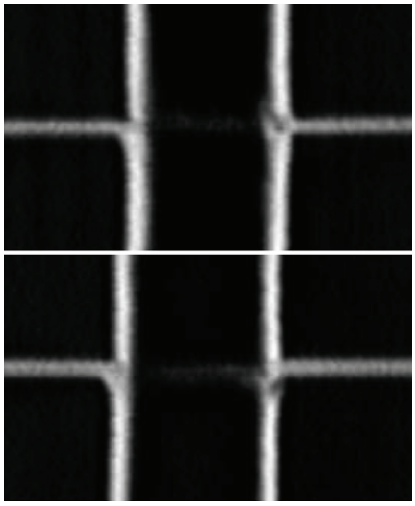

(b) Ω1 upper and lower intersections (defects 1 and 2)

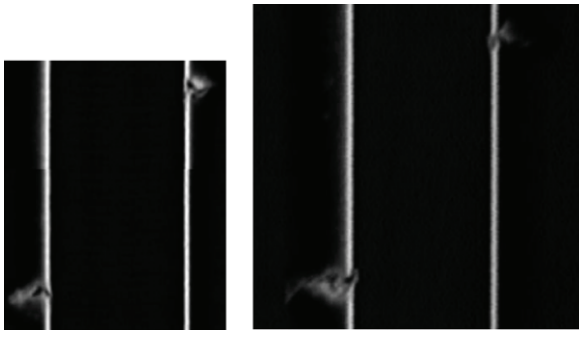

(c) Ω2 and Ω3 crippling failures (defects 3 and 4)

Fig. 22. Two-dimensional X-ray measurements.

The whole surface should be coloured in dark green for a skin thickness of about 2.2 mm, as well as the delaminated flange areas of Ω2 and Ω3. As locally there is a yellow–orange colour, one can conclude that decohesion is a kind of delamination phenomenon as delamination does not only propagate at skin-stiffener interface but locally inside the first two skin plies.

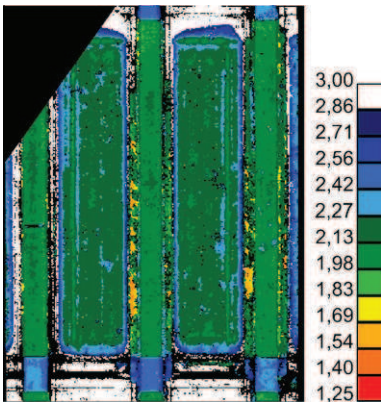

Fig. 23. US cartography of the decohesion interface distance to the skin (mm).

4. Conclusions

Numerical models have correctly predicted the experimental post-buckling test of this composite fuselage representative panel. The numerical approach previously followed [7] is validated.

Two experimental load drops are observed. The first load drop corresponds to Ω1 collapse with a failure at its intersections, confirmed by tomographic measurements. No stiffener moves apart the skin at the first load drop.

The second load drop is the Ω2 and Ω3 delamination, initiated by crippling, also underlighted by tomographic measurements.

Ultrasonic testing has shown the decohesion is a kind of delamination phenomenon, as it propagates locally in the first skin plies. That shows a very good assembly between the integrated structures and the skin. Therefore structures integrated by a resin infusion manufacturing process show a very good behaviour and are promising in comparison with structures manufactured using prepregs.

Prediction of Ω1 intersection failures is a limitation of the numerical models, as failure localisation is quite sensitive to how connection between integrated structures is modelled [7]: modelling connection with coincident nodes and sliding surfaces are two viable methods which can both give accurate results, depending on ply lay up and material properties. How intersections mechanically interact on the structure is not already known and could not be accurately modelled for the moment.

To deal with the decohesion propagation locally once delamination is initiated by crippling, integrated structures could be modelled using cohesive surfaces and traction-separation laws, with the help of out-of-plane material properties. Then cohesive surfaces could be used in the obvious debonding area.

However, the numerical approach is now validated and can be applied to larger models (fuselage type for example), with a linear buckling analysis to identify critical areas, where a local structure can buckle, followed by nonlinear models to give the global behaviour of the structure up to collapse.

References

[1] Zimmermann R, Klein H, Kling A. Buckling and postbuckling of stringer stiffened fibre composite curved panels – tests and computations. Compos Struct 2006;73:150–61.
[2] Bertolini J, Castani B, Barrau JJ, Navarro JP. Multi-level experimental and numerical analysis of composite stiffener debonding. Part 1: Non-specific specimen level. Compos Struct 2009.
[3] Krueger R, Ratcliffe J, Minguet P. Panel stiffener debonding analysis using a shell/3d modeling technique. Compos Sci Technol 2009;69(14):2352–62.
[4] Ambur DR, Rouse M. Design and evaluation of composite fuselage panels subjected to combined loading conditions. J Aircr 2005;42(4):1037–45.
[5] Stevens K, Ricci R, Davies G. Buckling and postbuckling of composite structures. Composites 1995;26(3):189–99.
[6] Falzon B, Stevens K, Davies G. Postbuckling behaviour of a blade-stiffened composite panel loaded in uniaxial compression. Compos Part A: Appl Sci Manuf 2000;31(5):459–68.
[7] Perret A, Mistou S, Fazzini M. Global behaviour of a composite stiffened panel in buckling. Part 1: Numerical modelling. Compos Struct 2011;93(10):2610–8.
[8] Perret A. Study of the post-buckling behaviour of a composite fuselage panel infused with integrated structures. Ph.D. Thesis; Université de Toulouse; 2011.
[9] Orifici A, Thomson R, Degenhardt R, Kling A, Rohwer K, Bayandor J. Degradation investigation in a postbuckling composite stiffened fuselage panel. Compos Struct 2007;82:217–24.
[10] Degenhardt R, Kling A, Rohwer K, Orifici A, Thomson R. Design and analysis of stiffened composite panels including post-buckling and collapse. Comput Struct 2008;86:919–29.
[11] FAR23 Federal Aviation Regulations. Part 23 – Airworthiness standards: normal, utility, acrobatic, and commuter category airplanes; 1987.
[12] Bertolini J. Contribution l'analyse experimentale et thorique des ruptures de structures composites en post-flambement par dcollement des raidisseurs. Ph.D. Thesis; UPS; 2008.